Nonequilibrium scaling of drag forces in counterdriven fluid mixtures

Jonas Köglmayr,[1] Florian Sammüller,[1] and Matthias Schmidt[1,*]

[1] *Theoretische Physik II, Physikalisches Institut, Universität Bayreuth, D-95447 Bayreuth, Germany*

(Dated: 29 May 2026)

We address the effective nonequilibrium drag force field that emerges from the microscopic interparticle interactions in steady states of counterdriven binary fluid mixtures. Using power functional scaling arguments for adaptive Brownian dynamics computer simulation results, we establish quantitatively the crossover between near-equilibrium linear response and far-nonequilibrium square root asymptotics. An algebraic expression captures both limiting cases and remains applicable in the crossover regime. Using simulation results as benchmarks, we verify that a local power functional approximation based on the scaling law reproduces the spatial nonequilibrium structure formation in inhomogenously driven systems. The crossover scenario transcends dynamical density functional theory and it sheds light on general nonequilibrium scaling of driven fluids.

The physics of fluid mixtures can be considerably richer than the phenomenology that pure, one-component systems display [1]. Recently studied collective phenomena that are specific to multi-component systems include composition-dependent phase instabilities [2, 3] and mobility effects in nonequilibrium [4]. When the two particle species in a *binary* mixture are driven in opposite directions, then a range of nonequilibrium structure formation effects occur, including laning and jamming [5–9]. To find fluid-fluid phase separation in equilibrium requires typically the presence of interparticle attraction, with the physics of liquid-liquid and liquid-gas phase transitions and their associated interfacial wetting phenomena being systematically accessible via equilibrium density functional theory [10–13]. Binary Lennard-Jones models [14–16] are prototypical [10–16] and these were used recently to demonstrate machine learning of accurate equilibrium density functionals that extrapolate significantly beyond the physics encountered during the simulation-based training [17, 18], as also demonstrated for electrolytes [19, 20].

The effective forces that generate nonequilibrium laning were analyzed [9] according to power functional theory [21]. This universal approach for general nonequilibrium dynamics is based on a formally exact one-body minimization principle. Workable approximations for the central functional dependencies were constructed analytically to describe the dependence on the velocity gradient of the occurring flow patterns [22–24], nonlocal memory convolution kernels [25–27], and the behaviour under shear [28]. The recent machine learning of neural nonequilibrium force functionals [29, 30] allows one in particular to go beyond the limitations of dynamical density functional theory [31, 32], which is a currently much used approach, see e.g. Refs. [33–35].

Here we aim to make progress in the description of nonequilibrium fluids by investigating the specific type of flows that occur in counterdriven binary mixtures. We consider both spatially homogeneous and inhomogeneous systems over a broad range of dilute and dense conditions under weak and strong driving. While we scan a wide set of parameter choices, we avoid deliberately those regimes where laning and jamming effects occur [5–9], and aim for a full quantitative description of the drag force field that emerges from the interparticle collisions between two counterflowing fluid species. We identify a well-characterized crossover regime that connects near-equilibrium linear response with far-nonequilibrium scaling that we identify under strong driving. The scaling of the drag force as a function of the counterflow velocity is linear near equilibrium and it has square-root dependence far in nonequilibrium. The development of the nonequilibrium scaling theory is based solely on analyzing systems that are spatially homogeneous, such that the two partial (i.e. species-resolved) density profiles are spatially constant. In such situations, dynamical density functional theory predicts per construction vanishing mean interparticle forces and hence it will not account for the observations. In contrast power functional scaling gives accurate quantitative account of the drag forces and we demonstrate that the approach transcends the homogeneous driving conditions and describes quantitatively spatially inhomogenenous nonequilibrium.

We use overdamped Brownian dynamics [1, 36] to model the microscopic many-body dynamics of the counterflowing mixture and implement the trajectory-based stochastic Langevin equations via adaptive Brownian dynamics simulations [37]. For overdamped dynamics the only relevant microscopic degrees of freedom are the positions $\mathbf{r}_1, \ldots, \mathbf{r}_N \equiv \mathbf{r}^N$ of the N particles, with $\mathbf{r}^N$ being a shorthand notation for all particle coordinates. To discriminate between the different species we use index sets $\mathcal{N}_\alpha$ that contain all particle indices i that belong to species $\alpha = 1, 2$ in the binary mixtures. The system is driven out of equilibrium by species-resolved external force fields $\mathbf{f}_{\mathrm{ext}}^{(\alpha)}(\mathbf{r})$ that couple individually to each species α. We are interested in steady states, where all mean one-body quantities depend on position $\mathbf{r}$ and are independent of time t. The reduction from three-dimensional to planar geometry is specified later.

The interparticle repulsion is modelled by the Weeks-Chandler-Andersen pair potential, which is a truncated

and shifted, purely repulsive Lennard-Jones potential given by $\phi(r) = 4\epsilon[(\sigma/r)^{12} - (\sigma/r)^6] + \epsilon$ for $r < 2^{1/6}\sigma$ and zero otherwise; ϵ is the energy scale and the lengthscale σ sets the particle size. The particles of the two different species share the same interaction potential, hence we consider a 'painted particle' model [2, 9], where the interparticle potential is $u(\mathbf{r}^N) = \sum_{i,j(\neq i)} \phi(|\mathbf{r}_i - \mathbf{r}_j|)/2$. The individual species are solely discriminated by the strength and the spatial form of the external force fields $\mathbf{f}_{\rm ext}^{(\alpha)}(\mathbf{r})$ that act on the different species $\alpha = 1, 2$. We use adaptive Brownian dynamics simulations [37] in a three-dimensional periodic cubic simulation box with linear size $L = 10\sigma$ and consider partial particle numbers in the range $N_\alpha = 30 - 300$ for each species $\alpha = 1, 2$. The temperature T is set such that $k_B T/\epsilon = 0.5$, where k_B denotes Boltzmann's constant. For each pair of partial density values considered, we realize 50 different driving strengths. For each system, after an initial relaxation period, steady state properties are sampled for a duration of 1000τ, where $\tau = \sigma^2\gamma/\epsilon$ is the microscopic time scale, with γ the common friction constant and $D = k_B T/\gamma$ the associated free diffusion constant.

We base the statistical mechanical description of the system on the dynamical one-body picture [1, 21]. The primary observables of interest are the partial density profile $\rho_\alpha(\mathbf{r})$ and the partial interparticle force density $\mathbf{F}_{\rm int}^{(\alpha)}(\mathbf{r})$. These are respectively defined as [21]:

$$\rho_\alpha(\mathbf{r}) = \Big\langle \sum_{i\in\mathcal{N}_\alpha} \delta(\mathbf{r} - \mathbf{r}_i) \Big\rangle, \tag{1}$$

$$\mathbf{F}_{\rm int}^{(\alpha)}(\mathbf{r}) = -\Big\langle \sum_{i\in\mathcal{N}_\alpha} \delta(\mathbf{r} - \mathbf{r}_i) \nabla_i u(\mathbf{r}^N) \Big\rangle, \tag{2}$$

where the angles denote the steady state average, the sums are over (only) particles indices $i \in \mathcal{N}_\alpha$ to ensure the correct attribution to species $\alpha = 1, 2$, the symbol $\delta(\cdot)$ indicates the Dirac distribution, and ∇_i is the derivative with respect to particle position $\mathbf{r}_i$. In general, imposing an external force field generates mean motion, which is characterized by nonvanishing one-body partial currents $\mathbf{J}_\alpha(\mathbf{r})$. For overdamped Brownian systems the partial current is induced by species-resolved diffusive, interparticle, and external contributions according to the force density balance [21]:

$$\gamma \mathbf{J}_\alpha(\mathbf{r}) = -k_B T \nabla \rho_\alpha(\mathbf{r}) + \mathbf{F}_{\rm int}^{(\alpha)}(\mathbf{r}) + \rho_\alpha(\mathbf{r}) \mathbf{f}_{\rm ext}^{(\alpha)}(\mathbf{r}). \tag{3}$$

For steady states the partial currents are divergence free, as follows from the continuity equation $\nabla \cdot \mathbf{J}_\alpha(\mathbf{r}) = -\partial \rho_\alpha(\mathbf{r})/\partial t = 0$. The partial velocity profile of species α is the ratio $\mathbf{v}_\alpha(\mathbf{r}) = \mathbf{J}_\alpha(\mathbf{r})/\rho_\alpha(\mathbf{r})$. Power functional theory ascertains [21] that $\mathbf{F}_{\rm int}^{(\alpha)}(\mathbf{r}, [\rho_1, \rho_2, \mathbf{v}_1, \mathbf{v}_2])$ is a universal functional of the partial density and velocity profiles, as is indicated in the notation by the square brackets. The dependence on these fields is causal and the universality refers to the absence of any functional dependence on the external force fields $\mathbf{f}_{\rm ext}^{(1)}(\mathbf{r})$ and $\mathbf{f}_{\rm ext}^{(2)}(\mathbf{r})$. That this type of functional dependence holds is a nontrivial result that is not apparent from Eq. (3) alone. We recall that power functional theory is the extension of classical

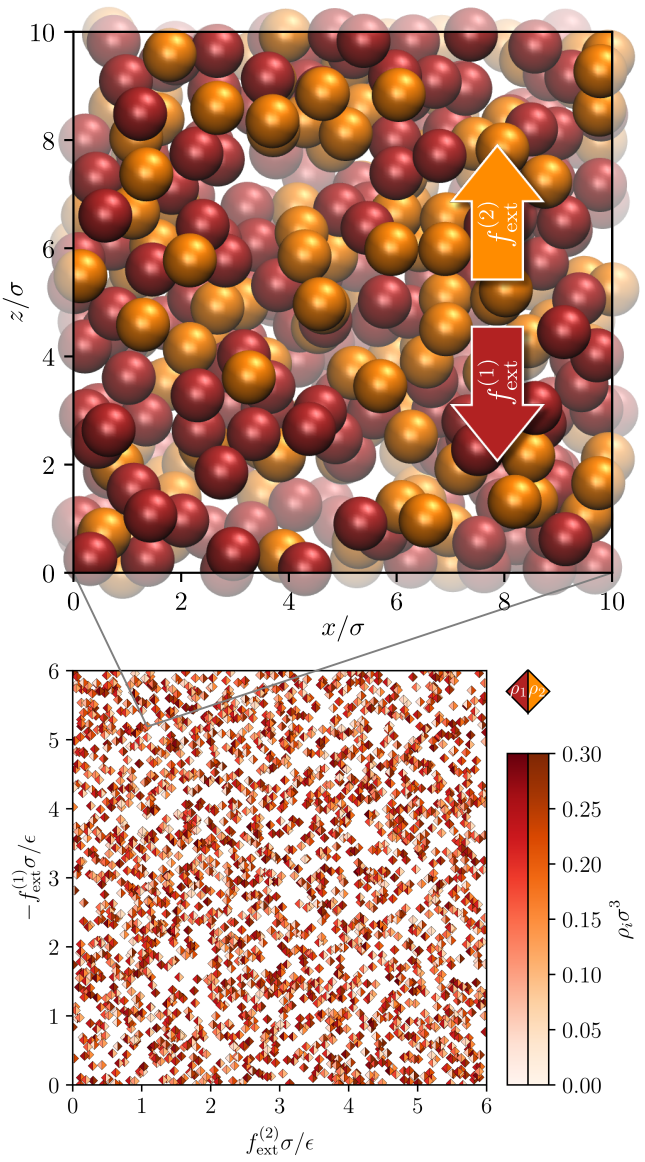

FIG. 1. Top panel: Representative simulation snapshot of the binary mixture under counterdrive. The particles of species 1 (dark red spheres) and of species 2 (light orange spheres) are driven in opposite directions along the z-axis by species-dependent external force fields $f_{\rm ext}^{(1)}(z)$ and $f_{\rm ext}^{(2)}(z)$, which are first taken to be spatially uniform and are later considered to be position-dependent on the z-coordinate. The system is on average homogeneous in the lateral x- and y-directions and lengths are scaled with the common particle size σ. Bottom panel: Illustration of the range of simulated systems with spatially homogeneous driving, shown across the plane of scaled force constants $f_{\rm ext}^{(1)}\sigma/\epsilon$ and $f_{\rm ext}^{(2)}\sigma/\epsilon$ with colour-coded partial densities $\rho_1\sigma^3$ and $\rho_2\sigma^3$ (semi-diamond symbols).

density functional theory [31], which establishes that in equilibrium, the internal force profile is a universal functional of (only) the densities, $\mathbf{F}_{\rm int}^{(\alpha)}(\mathbf{r},[\rho_1,\rho_2])$.

We first follow Geigenfeind *et al.* [9] to decompose the species-resolved interparticle force densities (2) into two separate contributions. Thereby the species-independent interparticle force field $\mathbf{f}_{\rm int}(\mathbf{r})$ is defined as the contribution that acts identically on both species. The counterforce ("differential force" [9]) density $\mathbf{G}_{\rm int}(\mathbf{r})$ acts on the relative motion between the two species. This decomposition constitutes a change of variables from $\mathbf{F}_{\rm int}^{(1)}(\mathbf{r})$ and $\mathbf{F}_{\rm int}^{(2)}(\mathbf{r})$ to $\mathbf{f}_{\rm int}(\mathbf{r})$ and $\mathbf{G}_{\rm int}(\mathbf{r})$, which is defined by:

$$\mathbf{F}_{\rm int}^{(\alpha)}(\mathbf{r}) = \rho_\alpha(\mathbf{r})\mathbf{f}_{\rm int}(\mathbf{r}) \pm \mathbf{G}_{\rm int}(\mathbf{r}), \quad \alpha = 1,2, \tag{4}$$

where $\pm$ refers to species $\alpha = 1,2$. By summing over both species in Eq. (4) one obtains by construction the total interparticle force density $\mathbf{F}_{\rm int}(\mathbf{r}) = \mathbf{F}_{\rm int}^{(1)}(\mathbf{r}) + \mathbf{F}_{\rm int}^{(2)}(\mathbf{r}) = \rho(\mathbf{r})\mathbf{f}_{\rm int}(\mathbf{r})$, with the total density profile $\rho(\mathbf{r}) = \rho_1(\mathbf{r}) + \rho_2(\mathbf{r})$. The counterforce density $\mathbf{G}_{\rm int}(\mathbf{r})$ follows correspondingly by subtraction (and multiplication by 1/2) and thus [9]:

$$\mathbf{f}_{\rm int}(\mathbf{r}) = \mathbf{F}_{\rm int}(\mathbf{r})/\rho(\mathbf{r}), \tag{5}$$

$$\mathbf{G}_{\rm int}(\mathbf{r}) = \left[\rho_2(\mathbf{r})\mathbf{F}_{\rm int}^{(1)}(\mathbf{r}) - \rho_1(\mathbf{r})\mathbf{F}_{\rm int}^{(2)}(\mathbf{r})\right]/\rho(\mathbf{r}). \tag{6}$$

In our planar geometrical setup we consider single-phase systems under the influence of external force fields $\mathbf{f}_{\rm ext}^{(\alpha)}(\mathbf{r}) = f_{\rm ext}^{(\alpha)}(z)\mathbf{e}_z$, where $\mathbf{e}_z$ is the unit vector in the z-direction. In the chosen geometry the particles move with mean velocity $\mathbf{v}_\alpha(z) = v_\alpha(z)\mathbf{e}_z$. The counterforce density acts parallel to the motion, $\mathbf{G}_{\rm int}(\mathbf{r}) = G_{\rm int}(z)\mathbf{e}_z$, and it represents the emerging drag that the particles of the two oppositely moving species exert onto each other. The general power functional dependence simplifies to $G_{\rm int}(z;[v_\Delta,\rho_1,\rho_2])$, where the velocity difference $v_\Delta(z) = v_2(z) - v_1(z)$ is a measure of the degree of the counterflow in the system. We first consider cases with force amplitudes $f_{\rm ext}^{(\alpha)}(z) = \text{const}$, such that also the partial density profiles $\rho_\alpha(z) = \text{const}$. For such homogeneous systems, as are illustrated in Fig. 1, it follows that also $G_{\rm int}(z) = \text{const}$. As all pertinent quantities are spatially constant in the considered homogeneous case, the functional dependence simplifies to a *parametric* dependence: $G_{\rm int}(z;[v_\Delta,\rho_1,\rho_2]) = \mathcal{G}(v_\Delta,\rho_1,\rho_2)$

To make progress, we propose the following ansatz for the scaling behavior of the uniform drag force density:

$$\mathcal{G}(v_\Delta,\rho_1,\rho_2) = \gamma\rho_s v_s \sqrt{\ln\cosh\left(v_\Delta/v_s\right)}\,\operatorname{sgn} v_\Delta, \tag{7}$$

and we lay out a justification based on asymptotics below. In the ansatz (7) the velocity scale $v_s(\rho_1,\rho_2)$ and the effective density $\rho_s(\rho_1,\rho_2)$ are as-yet unknown functions. These encapsulate the dependence on the partial densities ρ_1 and ρ_2 and these functions play decisive roles

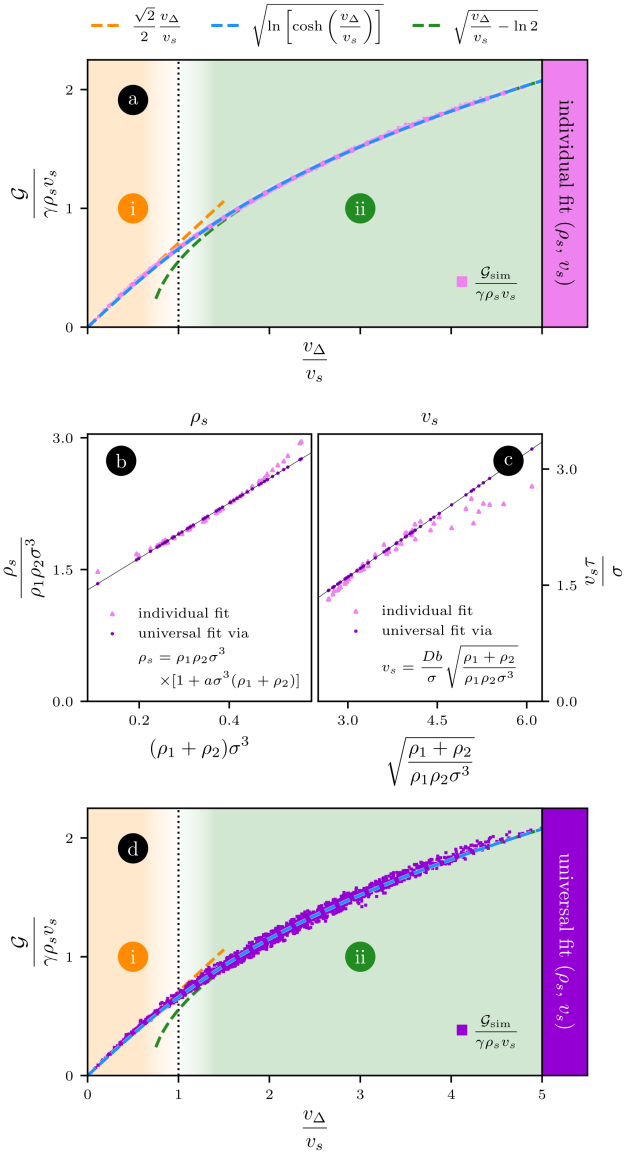

FIG. 2. Nonequilibrium scaling of drag forces. a) Drag force ratio $\mathcal{G}/(\gamma\rho_s v_s)$ shown as a function of the counterdrive velocity ratio v_Δ/v_s. Simulation results are obtained over wide ranges of partial densities and driving strengths, see Fig. 1. The 'individual fit' results (pink data points) collapse onto the general scaling function (7) (dashed blue curve). Indicated is the asymptotic behaviour for i) near-equilibrium (dashed orange) and ii) far-nonequilibrium (dashed green), see Eq. (8). b) Scaled effective density $\rho_s/(\rho_1\rho_2\sigma^3)$ as a function of the scaled total density $(\rho_1+\rho_2)\sigma^3$, obtained from the individual fits (pink symbols) and for the 'universal fit' (thin black line), where the data points (violet symbols) agree by construction with Eq. (9). c) Same as b) but for the scaled crossover velocity $v_s\tau/\sigma$ as a function of $\sqrt{(\rho_1+\rho_2)/(\rho_1\rho_2\sigma^3)}$ and compared against Eq. (10). d) Same as a) but obtained from the universal fit. Despite some scatter the correct scaling is retained.

in the behaviour of the scaling relationship (7). The ve-

locity scale v_s determines where the regimes of low- and high-drive behaviour cross over. The effective particle density ρ_s governs the overall amplitude of the drag force density (7). The spatial symmetry is odd, such that reversing the flow direction reverses the direction of the drag force density, $\mathcal{G}(-v_\Delta, \rho_1, \rho_2) = -\mathcal{G}(v_\Delta, \rho_1, \rho_2)$.

The scaling function (7) allows one to match simultaneously the behaviour in both the near-equilibrium and far-nonequilibrium regimes, as we demonstrate in the following. We first address the near-equilibrium behaviour and thus Taylor expand Eq. (7) in the small parameter $x = v_\Delta/v_s$. To lowest order this gives $\sqrt{\ln\cosh x} = \sqrt{\ln(1 + x^2/2 + O(x^4))} = \sqrt{x^2/2 + O(x^4)} = |x|/\sqrt{2} + O(x^3)$. We hence obtain the simple linear-response result $\mathcal{G}(v_\Delta; \rho_1, \rho_2) \sim \gamma\rho_s v_\Delta$, where the tilde indicates equality in the scaling regime. We recall that $\rho_s(\rho_1, \rho_2)$ is independent of v_Δ. Thus the near-equilibrium behaviour is independent of the crossover velocity v_s and bears no traces of its restricted validity towards the nonlinear regime.

We address the far-nonequilibrum behaviour by performing an asymptotic expansion of Eq. (7) for $x \to \pm\infty$, as follows from approximating the hyperbolic cosine: $\sqrt{\ln\cosh x} \sim \sqrt{\ln(\mathrm{e}^{|x|}/2)} = \sqrt{|x| - \ln 2}$. The resulting far-nonequilibrium form of Eq. (7) is $\mathcal{G} \sim \gamma\rho_s v_s\sqrt{|v_\Delta|/v_s - \ln 2}\,\mathrm{sgn}\, v_\Delta$. For high counterflow, $v_\Delta/v_s \to \pm\infty$, the dominant term is $\gamma\rho_s v_s\sqrt{|v_\Delta|/v_s}\,\mathrm{sgn}\, v_\Delta$. Notably the dependence on the crossover velocity v_s is retained in this limit. This implies that from studying the far-nonequilibrium behaviour only, one can infer its range of validity towards the near-equilibrium regime. Summarizing the above results for the low- and high-flow regimes, we have

$$\frac{\mathcal{G}(v_\Delta, \rho_1, \rho_2)}{\gamma\rho_s v_s} \sim \begin{cases} v_\Delta/v_s & |v_\Delta| \ll v_s \\ \sqrt{|v_\Delta|/v_s - \ln 2}\,\mathrm{sgn}\, v_\Delta & v_s \ll |v_\Delta|, \end{cases} \tag{8}$$

where we recall the tilde to indicate equality in the respective scaling regime.

We illustrate the different regimes by plotting the ratio $\mathcal{G}(v_\Delta, \rho_1, \rho_2)/(\gamma\rho_s v_s)$ in full form (7), together with its two asymptotically leading expansions (8), as a function of the scaled velocity difference v_Δ/v_s in Fig. 2a. The results from our adapative Brownian dynamics simulations are obtained under spatially constant driving conditions over considerable ranges of values of the partial densities ρ_1 and ρ_2, which vary independently from $0.03\sigma^{-3}$ to $0.30\sigma^{-3}$, and with different driving strengths $f_{\mathrm{ext}}^{(\alpha)}$ up to $6\epsilon/\sigma$, as depicted in Fig. 1.

To connect the theory quantitatively with the simulation results we first build subsets of all simulated systems that share the same pair of bulk density values ρ_1 and ρ_2. In each subset we treat the two scaling parameters ρ_s and v_s as 'individual fit' parameters to describe the counterflow behaviour in the subset. The resulting agreement of the simulation data with the scaling form (7) is near-perfect, see Fig. 2a. Similarly good agreement of the theoretical model and the simulation results, with some slight increase in scatter that is apparent in Fig. 2d, is obtained from the following alternative 'universal fit'.

The universal fit is obtained by observing that the dependence of the scaling parameters ρ_s and v_s on the partial densities ρ_1 and ρ_2 turns out to be relatively simple. We show in Fig. 2b the behaviour of the scaled crossover density $\rho_s/(\rho_1\rho_2\sigma^3)$ as a function of the scaled total density $(\rho_1 + \rho_2)\sigma^3$. Correspondingly we show in Fig. 2c the scaled crossover velocity $v_s\tau/\sigma$ as a function of the density combination $\sqrt{(\rho_1 + \rho_2)/(\rho_1\rho_2\sigma^3)}$. In both cases linear behaviour is found, which can be *quantitatively* represented by the following simple 'universal fit' forms:

$$\rho_s(\rho_1, \rho_2) = \rho_1\rho_2[1 + a(\rho_1 + \rho_2)\sigma^3]\sigma^3, \tag{9}$$

$$v_s(\rho_1, \rho_2) = \frac{Db}{\sigma}\sqrt{\frac{\rho_1 + \rho_2}{\rho_1\rho_2\sigma^3}}. \tag{10}$$

Here $a\sigma^3$ constitutes an interaction volume that connects the partial densities with the effective density ρ_s and b/σ is an inverse interaction length scale that relates the free diffusion constant (we recall $D = k_BT/\gamma$) to the crossover velocity v_s. We obtain the parameter values $a = 3.14$ and $b = 1.07$ from a least-squares fit across our entire data set. The thin black lines in Fig. 2b, c indicate these choices in Eqs. (9) and (10). Despite some outliers and the agreement worsening slightly for very dissimilar partial densities, the full behaviour of the simulation results is captured quantitatively by the analytical forms (9) and (10).

We next compare the results of the analytical counterforce model, as given by the scaling form (7) of $\mathcal{G}(v_\Delta, \rho_1, \rho_2)$ and the parameter dependencies (9) and (10), against the results of all our simulations. Although the simple expressions (9) and (10) introduce some deviations from the simulations results, the overall level of agreement is very satisfactory, see Fig. 2d. We recall the large parameter space that is explored by the simulations, as illustrated in Fig. 1. The overall 'universal' model (7), (9) and (10) thus contains merely two empirical parameters a and b and it captures quantitatively the *entirety* of our simulation results for homogeneous conditions near to and far from equilibrium.

We use the validity of this analytical model for conditions of spatially homogeneous drive as an outset to develop a theory that captures long-ranged spatial variation in terms of a local power functional approximation. We address two representative model situations. The first, 'co-modulated' case is colour-blind such that the constant counterdrive $\pm f_0$ is supplemented by a modulated force field that is identical for both species. The external force fields are $f_{\mathrm{ext}}^{(\alpha)}(z) = \pm f_0 - f_1\sin(2\pi z/L)$, where f_0 is the offset, f_1 is an amplitude parameter, and $\pm$ refers to species $\alpha = 1, 2$. In the second, 'counter-modulated' case the entire external force acts in opposite

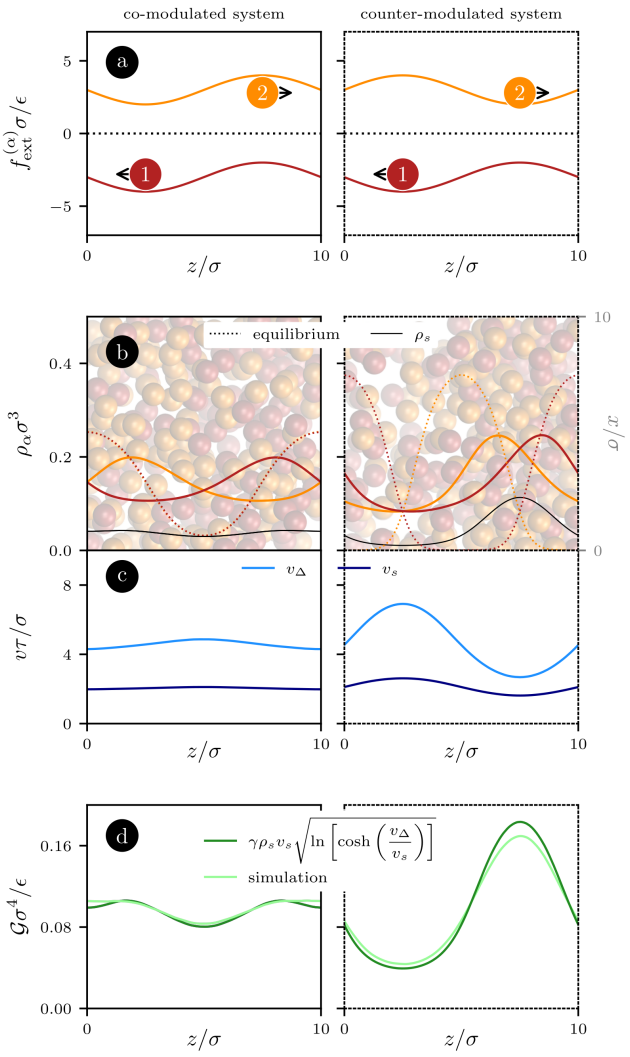

FIG. 3. Inhomogeneous systems with co-modulated (left column) and counter-modulated driving (right column) along the z-direction. a) The inhomogeneous external force fields $f_{\rm ext}^{(\alpha)}(z)\sigma/\epsilon$ for species $\alpha = 1$ (dark red) and 2 (light orange). b) The resulting species-resolved nonequilibrium density profiles $\rho_1(z)\sigma^3$ and $\rho_2(z)\sigma^3$ together with the corresponding equilibrium density profiles (dashed lines) and the local scaling density $\rho_s(z)\sigma^3$ (black line). The background shows representative simulation snapshots (with horizontal z-direction) to illustrate the spatial concentration and density variations. c) The local velocity difference profile $v_\Delta(z)\tau/\sigma$ (light blue line), as obtained from simulations, together with the local scaling velocity $v_s(z)\tau/\sigma$ (dark blue line). d) The relative motion of the two species is well described by the drag force density $\mathcal{G}(z)\sigma^4/\epsilon$ obtained from the local power functional (11) (dark green lines), as confirmed by comparison to simulation results (light green lines).

directions for both species, which is akin to a symmetric electrolyte in an electric field. The external force fields are $f_{\rm ext}^{(\alpha)}(z) = \pm f_0 \pm f_1 \sin(2\pi z/L)$. In both cases the two species are driven against each other by the constant force $\pm f_0$. We show representative results for $f_0 = 3\epsilon/\sigma$ and $f_1 = 1\epsilon/\sigma$.

In the co-modulated system (Fig. 3, left column) the drag force exhibits weak spatial variation that displays maxima in the regions of maximal density difference between the two species. The counter-modulated system (Fig. 3, right column) displays much stronger modulation of the density contrast, as one might expect from the setup. The counterflow acts to move the two density maxima much closer together than they are in equilibrium ($f_0 = 0$). The spatial region around the two partial density maxima has a strong peak in the local drag force density. The shape of the peak is spatially more localized than the shallow minimum that occurs in the region of relative density depletion.

We rationalize these simulation results on the basis of a theoretical model for *inhomogeneous* counterflow based on the above scaling forms (7), (9), and (10) that were identified for homogeneous drive. We use a local power functional approximation, where we let the scaling parameters depend on the partial density profiles via localized versions of Eqs. (9) and (10), such that the local density scale is $\rho_s(z) = \rho_s(\rho_1(z), \rho_2(z))$, and the local crossover velocity is $v_s(z) = v_s(\rho_1(s), \rho_2(s))$. This allows one to express a local approximation of the universal scaling function (7) in the form:

$$\mathcal{G}(z) = \mathcal{G}\big(v_\Delta(z), \rho_1(z), \rho_2(z)\big). \tag{11}$$

When compared against simulation results, the local power functional approximation (11) performs very satisfactorily, as is shown for the two representative inhomogeneous systems in Fig. 3. The scaling model captures correctly the physics of inhomogeneous conditions via the power functional dependence of the mean interparticle force field on the counterflow velocity. Any mere dynamical density functional dependence misses the effect by construction.

In conclusion we have presented simulation-based evidence for the nonequilibrium scaling of drag forces in driven mixtures. For the considered steady states our results confirm the existence of the power functional map [21, 38, 39] from the partial density and velocity profiles to the localized one-body force densities via the explicit functional independence on the external forces. Based on a systematic force decomposition [9], our work goes beyond previous efforts in modelling the functional dependencies. Here we have identified both near-equilibrium and far-nonequilibrium regimes and elucidated quantitatively the intervening crossover behaviour. Future work could address the possible generality of the proposed scenario beyond counterflow and consider methods for first-principles derivations as well as nonequilibrium functional machine learning [29, 30], where binary mixtures have been addressed successfully in equilibrium [17–20]. It is also interesting to investigate the significance of our findings in light of currrent research dedicated to the

physics of responsive colloidal particles that can adapt their interparticle forces through a variety of different influences and across varying physical situations [40–45]. As our methodology rests firmly on the one-body force balance equation and functional concepts, it could be highly rewarding to relate the present findings to hyperforces [46, 47] in the context of the recent gauge invariance of statistical mechanics [48–54].

Data availability—The data that support the findings of this study were generated by numerical simulations. The source code and parameters used to generate the simulations is publicly available [55].

We thank Silas Robitschko and Pia Fleischmann for useful discussions. Calculations were performed using the emil-cluster of the Bayreuth Center for High Performance Computing funded by the DFG (Deutsche Forschungsgemeinschaft) under project no. 422127126. This work is supported by the DFG (Deutsche Forschungsgemeinschaft) under project no. 551294732.

* Matthias.Schmidt@uni-bayreuth.de

[1] J. P. Hansen and I. R. McDonald, *Theory of Simple Liquids*, 4th ed. (Academic Press, London, 2013).
[2] F. C. Thewes, M. Krüger, and P. Sollich, Composition dependent instabilities in mixtures with many components, Phys. Rev. Lett. **131**, 058401 (2023).
[3] F. C. Thewes, M. Krüger, and P. Sollich, Mobility-induced kinetic effects in multicomponent mixtures, Europhys. Lett. **147**, 27001 (2024).
[4] M. Akaberian, F. C. Thewes, P. Sollich, and M. Krüger, Nonequilibrium mixture dynamics: A model for mobilities and its consequences, J. Chem. Phys. **158**, 214504 (2023).
[5] J. Dzubiella, G. P. Hoffmann, and H. Löwen, Lane formation in colloidal mixtures driven by an external field, Phys. Rev. E **65**, 021402 (2002).
[6] J. Chakrabarti, J. Dzubiella, and H. Löwen, Dynamical instability in driven colloids, Europhys. Lett. **61**, 415 (2003).
[7] J. Chakrabarti, J. Dzubiella, and H. Löwen, Reentrance effect in the lane formation of driven colloids, Phys. Rev. E **70**, 012401 (2004).
[8] H. Yu and R. L. Jack, Competition between lanes and transient jammed clusters in driven binary mixtures, Phys. Rev. E **109**, 024123 (2024).
[9] T. Geigenfeind, D. de las Heras and M. Schmidt, Superadiabatic demixing in nonequilibrium colloids, Commun. Phys. **3**, 23 (2020).
[10] M. M. Telo da Gama and R. Evans, The structure and surface tension of the liquid-vapour interface near the upper critical end point of a binary mixture of Lennard-Jones fluids: I. The two phase region, Mol. Phys. **48**, 229 (1983).
[11] M. M. Telo da Gama and R. Evans, The structure and surface tension of the liquid-vapour interface near the upper critical end point of a binary mixture of Lennard-Jones fluids: II. The three phase region and the Cahn wetting transition, Mol. Phys. **48**, 251 (1983).
[12] P. Tarazona, R. Evans, and U. Marini Bettolo Marconi, Pairwise correlations at a fluid-fluid interface: The influence of a wetting film, Mol. Phys. **54**, 1357 (1985).
[13] I. Hadjiagapiou and R. Evans, Adsorption from a binary fluid mixture: The composite wetting film at the solid-vapour interface, Mol. Phys. **54**, 383 (1985).
[14] N. B. Wilding, Critical end point behavior in a binary fluid mixture, Phys. Rev. E **55**, 6624 (1997).
[15] F. Schmid and N. B. Wilding, Wetting of a symmetrical binary fluid mixture on a wall, Phys. Rev. E **63**, 031201 (2001).
[16] N. B. Wilding and F. Schmid, Wetting of a symmetrical binary fluid mixture on a wall, Comp. Phys. Comm. **147**, 149 (2002).
[17] S. Robitschko, F. Sammüller, M. Schmidt, and R. Evans, Learning the bulk and interfacial physics of liquid-liquid phase separation with neural density functionals, J. Chem. Phys. **163**, 161101 (2025).
[18] K. L. Y. Zhou, A. T. Bui and S. J. Cox, The roles of bulk and surface thermodynamics in the selective adsorption of a confined azeotropic mixture, J. Phys. Chem. B **130**, 4455 (2026).
[19] A. T. Bui and S. J. Cox, Learning classical density functionals for ionic fluids, Phys. Rev. Lett. **134**, 148001 (2025).
[20] A. T. Bui and S. J. Cox, Dielectrocapillarity for exquisite control of fluids, Nat. Commmun. **17**, 2661 (2026).
[21] M. Schmidt, Power functional theory for many-body dynamics, Rev. Mod. Phys. **94**, 015007 (2022).
[22] N. C. X. Stuhlmüller, T. Eckert, D. de las Heras, and M. Schmidt, Structural nonequilibrium forces in driven colloidal systems, Phys. Rev. Lett. **121**, 098002 (2018).
[23] D. de las Heras and M. Schmidt, Velocity gradient power functional for Brownian dynamics, Phys. Rev. Lett. **120**, 028001 (2018).
[24] D. de las Heras and M. Schmidt, Flow and structure in nonequilibrium Brownian many-body systems, Phys. Rev. Lett. **125**, 018001 (2020).
[25] L. L. Treffenstädt and M. Schmidt, Memory-induced motion reversal in Brownian liquids, Soft Matter **16**, 1518 (2020).
[26] L. L. Treffenstädt and M. Schmidt, Universality in driven and equilibrium hard sphere liquid dynamics, Phys. Rev. Lett. **126**, 058002 (2021).
[27] L. L. Treffenstädt, T. Schindler, M. Schmidt, Dynamic decay and superadiabatic forces in the van Hove dynamics of bulk hard sphere fluids, SciPost Phys. **12**, 133 (2022).
[28] N. Jahreis and M. Schmidt, Shear-induced deconfinement of hard disks, Col. Pol. Sci. **298**, 895 (2020).
[29] D. de las Heras, T. Zimmermann, F. Sammüller, S. Hermann, and M. Schmidt, Perspective: How to overcome dynamical density functional theory, J. Phys.: Condens. Matter **35**, 271501 (2023).
[30] T. Zimmermann, F. Sammüller, S. Hermann, M. Schmidt, and D. de las Heras, Neural force functional for non-equilibrium many-body colloidal systems, Mach. Learn.: Sci. Technol. **5**, 035062 (2024).
[31] R. Evans, The nature of the liquid-vapour interface and other topics in the statistical mechanics of non-uniform, classical fluids, Adv. Phys. **28**, 143 (1979).
[32] M. te Vrugt, H. Löwen, and R. Wittkowski, Classical dynamical density functional theory: from fundamentals to applications, Adv. Phys. **69**, 121 (2020).

[33] R. D. Mills-Williams, B. D. Goddard, and A. J. Archer, Dynamic density functional theory with inertia and background flow, J. Chem. Phys. **160**, 174901 (2024).

[34] S. M. Tschopp and J. M. Brader, Superadiabatic dynamical density functional theory for colloidal suspensions under homogeneous steady-shear, J. Chem. Phys. **160**, 214124 (2024).

[35] K. Ram, J. Dijkman, R. van Roij, J.-W. van de Meent, B. Ensing, M. Welling, and D. Cremers, Learned free-energy functionals from pair-correlation matching for dynamical density functional theory, Phys. Rev. E **112**, 045314 (2025).

[36] J. K. G. Dhont, An Introduction to the Dynamics of Colloids (Elsevier, Amsterdam, 1996).

[37] F. Sammüller and M. Schmidt, Adaptive Brownian dynamics, J. Chem. Phys. **155**, 134107 (2021).

[38] M. Schmidt and J. M. Brader, Power functional theory for Brownian dynamics, J. Chem. Phys. **138**, 214101 (2013).

[39] J. M. Brader and M. Schmidt, Power functional theory for the dynamic test particle limit, J. Phys.: Condens. Matter **27**, 194106 (2015).

[40] A. Moncho-Jordá and J. Dzubiella, Controlling the microstructure and phase behavior of confined soft colloids by active interaction switching, Phys. Rev. Lett. **125**, 078001 (2020).

[41] M. Bley, J. Dzubiella, and A. Moncho-Jordá, Active binary switching of soft colloids: stability and structural properties, Soft Matter **17**, 7682 (2021).

[42] M. Bley, P. I. Hurtado, J. Dzubiella, and A. Moncho-Jordá, Active interaction switching controls the dynamic heterogeneity of soft colloidal dispersions, Soft Matter **18**, 397 (2022).

[43] U. Baul and J. Dzubiella, Structure and dynamics of responsive colloids with dynamical polydispersity, J. Phys.: Condens. Matter **33**, 174002 (2021).

[44] J. López-Molina, M. Tirado-Miranda, J. Dzubiella, and A. Moncho-Jordá, Density functional theory for responsive hard-sphere fluids, Mol. Phys. **122**, e2410481 (2024).

[45] A. Moncho-Jorda, N. Goeth, and J. Dzubiella, Liquid structure of bistable responsive macromolecules using mean-field density-functional theory, Soft Matter **19**, 2832 (2023).

[46] S. Robitschko, F. Sammüller, M. Schmidt, and S. Hermann, Hyperforce balance from thermal Noether invariance of any observable, Commun. Phys. **7**, 103 (2024).

[47] J. Matthes, S. Robitschko, J. Müller, S. Hermann, F. Sammüller, and M. Schmidt, Gauge invariance and hyperforce correlations in equilibrium fluid mixtures, J. Chem. Phys. **164**, 044903 (2026).

[48] S. Hermann and M. Schmidt, Noether's theorem in statistical mechanics, Commun. Phys. **4**, 176 (2021).

[49] J. Müller, S. Hermann, F. Sammüller, and M. Schmidt, Gauge invariance of equilibrium statistical mechanics, Phys. Rev. Lett. **133**, 217101 (2024).

[50] J. Müller, F. Sammüller, and M. Schmidt, Dynamical gauge invariance of statistical mechanics, arXiv:2504.17599.

[51] J. Müller, F. Sammüller, and M. Schmidt, Why gauge invariance applies to statistical mechanics, J. Phys. A: Math. Theor. **58**, 125003 (2025).

[52] T. Maruyama, T. Seto, V. Zaverkin, H. Christiansen, A Leibniz rule of distributional pairing and hyperforce sum rule, arXiv:2603.01519.

[53] N. Nguyen-Tran-Thanh, T. Nguyen-Xuan, and H. Pham-Van, Gauge theory of orientation in anisotropic fluids, Phys. Rev. E **113**, 025401 (2026).

[54] H. Pham-Van, Unified gauge-geometry symmetry for equilibrium statistical mechanics, Phys. Rev. E **113**, 054134 (2026).

[55] Simulation code and parameters available at `https://gitlab.uni-bayreuth.de/bt306964/mbd`.